

# Quantum spin-liquid emerging in two-dimensional correlated Dirac fermions

Z. Y. Meng<sup>1</sup>, T. C. Lang<sup>2</sup>, S. Wessel<sup>1</sup>, F. F. Assaad<sup>2</sup> & A. Muramatsu<sup>1</sup>

<sup>1</sup>*Institut für Theoretische Physik III, Universität Stuttgart, Pfaffenwaldring 57, 70550 Stuttgart, Germany*

<sup>2</sup>*Institut für Theoretische Physik und Astrophysik, Universität Würzburg, Am Hubland, 97074 Würzburg, Germany*

**At sufficiently low temperatures, condensed-matter systems tend to develop order. An exception are quantum spin-liquids, where fluctuations prevent a transition to an ordered state down to the lowest temperatures. While such states are possibly realized in two-dimensional organic compounds, they have remained elusive in experimentally relevant microscopic two-dimensional models. Here, we show by means of large-scale quantum Monte Carlo simulations of correlated fermions on the honeycomb lattice, a structure realized in graphene, that a quantum spin-liquid emerges between the state described by massless Dirac fermions and an antiferromagnetically ordered Mott insulator. This unexpected quantum-disordered state is found to be a short-range resonating valence bond liquid, akin to the one proposed for high temperature superconductors. Therefore, the possibility of unconventional superconductivity through doping arises. We foresee its realization with ultra-cold atoms or with honeycomb lattices made with group IV elements.**

The quantum mechanical description of the relativistic electron was attained by Dirac, who revealed both its intrinsic angular momentum (the spin), with a half-integer quantum number  $S = 1/2$ , and the existence of its antiparticle, the positron<sup>1</sup>. Both obey the Fermi-Dirac statis-

tics, which implies that two identical particles cannot occupy the same quantum mechanical state. Such particles are generically called fermions. In case of a vanishing rest mass, the energy of Dirac fermions is a linear function of momentum. Such massless Dirac fermions were recently observed in two-dimensional solid-state systems like graphene<sup>2,3</sup> and surfaces of bismuth based compounds<sup>4,5</sup>. For graphene, a single layer of carbon atoms with honeycomb structure, unusual electronic behaviour is anticipated, and partly verified experimentally, due to the two-dimensional Dirac-like dispersion of the electrons at low energies<sup>6</sup>. The interplay of a relativistic dispersion with interactions at half-filling is expected to lead to a quantum phase transition between the semimetal (SM) at low and a Mott insulator (MI) at high interaction strengths<sup>7,8</sup>. Here, a Mott insulator is an insulating state that results not from the band structure alone, but is due to the effects of interactions. Such correlation effects can be displayed by the Hubbard model in its most basic form, as exemplified in high temperature superconductivity<sup>9</sup>, or with ultra-cold fermionic atoms loaded in optical lattices<sup>10,11</sup>. Studies of Hubbard-like models on the honeycomb lattice suggested the emergence of exotic phases such as gapless spin liquids<sup>12,13</sup>, charge density waves<sup>14</sup>, quantum spin Hall states<sup>14,15</sup>, or superconductivity<sup>16</sup> at or near a density of one fermion per site (half-filling for the two-species case).

Given the various phases proposed for fermions on a honeycomb lattice based on Hubbard-like models, it is important to explore the ground-state properties in the intermediate coupling regime of the original lattice model with an unbiased method. Due to the absence of a sign-problem in determinantal quantum Monte Carlo (QMC) simulations (see Methods) in the half-filled case, it is the method of choice for extrapolations to the thermodynamic limit (TDL), leading to essentially exact results limited only by the statistical noise. Employing large-scale quantum Monte Carlo simulations of the spin- $\frac{1}{2}$  Hubbard model at half-filling on the honeycomb lattice, we show that for

intermediate interactions a gapped non-magnetic phase destroys the semimetal before the transition to an antiferromagnetically ordered Mott insulator at strong interactions sets in. This quantum spin-liquid phase is characterized by local correlations that correspond to a resonating valence-bond (RVB) state<sup>17,18</sup> as proposed in the context of high temperature superconductivity<sup>9,19,20</sup>.

Following their original proposals<sup>17-20</sup>, spin-liquid states were established in effective models of singlet-dynamics such as quantum dimer models<sup>21-23</sup>. Our results show that RVB states are realized in a microscopic model of correlated electrons, bringing closer their observation in experiments. Honeycomb lattices of group IV elements<sup>24</sup> and ultra-cold fermionic atoms loaded in optical lattices<sup>10,11,25</sup> appear as promising candidate systems to realize the RVB state out of Dirac fermions.

### **Phase diagram from quantum Monte Carlo**

Previous numerical studies of the Hubbard model on the honeycomb lattice<sup>26,27</sup> suggested that a single quantum phase transition separates the paramagnetic weak-coupling SM phase from a strong-coupling antiferromagnetic (AF) MI. At strong enough repulsion, antiferromagnetism is certainly possible since the honeycomb lattice is bipartite, so that AF order is not geometrically frustrated. However, the honeycomb lattice has the smallest coordination number in two dimensions, such that the effect of quantum fluctuations is the strongest. Hence, the competition between the tendency to order and quantum fluctuations requires a detailed analysis of correlations and a careful extrapolation to the TDL in order to characterize the possible phases. Here, we present results based on projective (temperature  $T = 0$ ) determinantal QMC simulations in the canonical ensemble at half-filling. In order to assess the above scenarios, we focus in particular on the region

near the Mott transition.

The Hamiltonian of the spin- $\frac{1}{2}$  Hubbard model on the honeycomb lattice equals

$$H = -t \sum_{\langle i,j \rangle, \alpha} (c_{i\alpha}^\dagger c_{j\alpha} + c_{j\alpha}^\dagger c_{i\alpha}) + U \sum_i n_{i\uparrow} n_{i\downarrow}, \quad (1)$$

where  $c_{i\alpha}^\dagger$  ( $c_{i\alpha}$ ) denotes the creation (annihilation) operator for fermions of spin  $\alpha = \uparrow, \downarrow$  on lattice site  $i$ , and  $n_{i\alpha} = c_{i\alpha}^\dagger c_{i\alpha}$ . Here,  $t$  denotes the nearest-neighbour hopping amplitude, and  $U \geq 0$  the strength of the onsite repulsion. Our notations in real and momentum space are shown in the inset of Fig. 1. At  $U = 0$ , the tight-binding Hamiltonian has a linear dispersion near the Dirac points ( $K, K'$  – cf. Fig. 1), where the conduction and valence bands touch at half-filling, corresponding to a density  $\sum_\alpha \langle n_{i\alpha} \rangle = 1$ . At half-filling, the finite- $U$  region can be studied using projective QMC to obtain ground-state expectation values of any physical observable. Details are relegated to the Methods section. The phases described in the following correspond to extrapolations to the TDL. For that purpose we study lattices of  $N = 2L^2$  sites with periodic boundary conditions, and linear sizes up to  $L = 18$ .

To monitor the electronic properties of the system upon increasing  $U$ , we extracted the single-particle excitation gap  $\Delta_{sp}(\mathbf{k})$  from the imaginary-time displaced Green's function (cf. Supplementary Information (SI) for details).  $\Delta_{sp}(\mathbf{k})$  gives the minimal energy necessary to extract one fermion from the system, and corresponds to the gap that can be observed in photoemission experiments. As shown in Fig. 1,  $\Delta_{sp}(K) = 0$  for  $U/t$  below about 3.5, as expected for a SM. For larger  $U/t$ , the system enters into an insulating phase due to interactions. The values of the gap are obtained via an extrapolation of the QMC data to the TDL as shown in Fig. 2a.

From previous analysis of the model, one expects long-range AF correlations when the MI

appears. We therefore measured the AF spin structure factor  $S_{AF}$  (cf. SI) that reveals long-range AF order if  $m_s^2 = \lim_{N \rightarrow \infty} S_{AF}/N > 0$ . Figure 2b shows the QMC results together with a finite size extrapolation. The results of the latter are also presented in the phase diagram of Fig. 1. AF order appears beyond  $U/t = 4.3$ , a value that is consistent with previous estimates for the onset of long-ranged AF order<sup>26,27</sup>. This leaves an extended window  $3.5 < U/t < 4.3$ , within which the system is neither a SM, nor an AF MI.

Further details on the nature of this intermediate region are obtained by examining the spin excitation gap, extracted from the long-time behaviour of the imaginary-time displaced spin-spin correlation function (cf. SI). We consider first the spin gap  $\Delta_s$  in the staggered sector at  $\mathbf{k} = \Gamma$ , which vanishes inside the AF phase due to the emergence of two Goldstone modes, as well as in the gapless SM phase. Figure 2c shows finite size estimates of  $\Delta_s$  for different values of  $U/t$ , along with an extrapolation to the TDL. A finite value of  $\Delta_s$  persists within an intermediate parameter regime  $3.5 < U/t < 4.3$ , while it vanishes both within the SM and the AF phase. This dome in the spin gap is also seen in the inset of Fig. 2c, that displays both the finite-size data and the extrapolated values of  $\Delta_s$  as a function of  $U/t$ . We also calculated the uniform spin gap  $\Delta_u$  by extrapolating the spin gap observed at the smallest finite  $\mathbf{k}$ -vector on each cluster to the TDL.  $\Delta_u$  is found to be even larger than  $\Delta_s$  inside the intermediate region (e.g.  $\Delta_u = 0.099 \pm 0.001$  (s.e.m.) at  $U/t = 4$ ), and vanishes in the SM and the AF phase ( $\Delta_u$  cannot be measured directly at  $\mathbf{k} = 0$ , because the uniform magnetization is a conserved quantity, cf. SI). Hence, this intermediate insulating region corresponds to a spin-gap phase.

From analysing the  $U$ -dependence of the kinetic energy density,  $E_{kin} = \langle -t \sum_{\langle i,j \rangle, \alpha} (c_{i\alpha}^\dagger c_{j\alpha} + c_{j\alpha}^\dagger c_{i\alpha}) \rangle / N$ , we obtain further insight into these different regimes and the emergence of local mo-

ments. As shown in Fig. 3, the curvature  $d^2 E_{kin}/dU^2$  changes sign near  $U/t = 4.3$ . This marks a characteristic change from the weak-coupling region of positive curvature with delocalized electrons to the strong-coupling AF region with negative curvature. In the latter region, localized spins form and order in an AF state. In the intermediate spin-gap region, fluctuations are large enough to still prevent the formation of well-localized magnetic moments. Note, that around  $U/t = 3.5$ , a change in the curvature can be observed, that adds to the already presented evidence for an intermediate phase.

### Characterization of the spin-gap phase

The observation of a finite spin gap rules out a gapless spin-liquid<sup>12,13</sup>, quantum spin Hall states<sup>14</sup>, as well as triplet superconductivity<sup>16</sup>. The remaining possibilities can be enumerated by considering the coupling to order parameters that lead to the opening of a mass gap in Dirac fermions<sup>28</sup>, and hence account for the single-particle gap observed in the QMC data: (i) singlet superconductivity, (ii) a quantum Hall state (QHS)<sup>29</sup>, (iii) charge density wave (CDW) order<sup>14</sup> and (iv) a valence bond crystal (VBC).

In order to assess if superconductivity arises in the vicinity of the Mott transition, we used the method of flux quantisation which probes the superfluid density and is hence independent of the specific symmetry of the pair wave function<sup>30</sup>. Let  $\Phi$  be a magnetic flux traversing the centre of a torus on which the electronic system lies and  $E_0(\Phi/\Phi_0)$  the total ground-state energy,  $\Phi_0$  being the flux quantum. A superconducting state of Cooper pairs is present if in the TDL, the macroscopic energy difference  $E_0(\Phi/\Phi_0) - E_0(\Phi/\Phi_0 = 1/2)$  is a function with period  $1/2$ <sup>31</sup>. In contrast, a metallic phase is characterized by  $E_0(\Phi/\Phi_0) - E_0(\Phi/\Phi_0 = 1/2)$  vanishing as a power law as a

function of system size, while in an insulating phase, it would vanish exponentially. As shown in the SI, this quantity vanishes in the TDL both in the semi-metallic state at  $U = 0$  and at  $U/t = 4$ , i.e. in the intermediate phase. In addition, we measured pair correlations, ruling out superconductivity in (extended)  $s$ -,  $p$ -,  $d$ -, and  $f$ -wave channels (cf. SI). Hence, both flux quantization as well as a direct measurement of pair correlations lead to no sign of superconductivity.

Both the CDW and QHS trigger a breaking of the sub-lattice symmetry and thereby open a mass gap at the mean-field level. A detailed analysis of the charge-charge correlation functions rules out a CDW. Furthermore, we find no signature for the presence of (spin) currents in the ground-state (cf. SI). This rules out the breaking of sublattice and time reversal symmetries, as required for the QHS, in the pristine Hubbard model, and possibly, extensions of it are necessary to reach such a state<sup>14</sup>.

To examine the occurrence of a VBC, we probed for dimer-dimer correlations between separated dimers formed by nearest neighbour bonds  $\langle ij \rangle$  and  $\langle kl \rangle$  (cf. SI). We find no VBC, neither in the charge, nor in the spin sector. Figure 4 shows the results of this measurement in the spin sector, i.e. the correlation between singlet dimers at  $U/t = 4.0$ . The striped bond is the one with respect to which correlations were determined. They are found to be short-ranged, and consistent with the dominance of a RVB state within the hexagons of the honeycomb lattice. This can be seen by comparing the singlet-correlations with those of an isolated hexagon (inset Fig. 4), the classical example of the resonance phenomenon in conjugated  $\pi$ -electrons<sup>32</sup>. Accordingly, we find no long-ranged order from the dimer-dimer structure factors in Fourier space. Our results thus reveal a genuinely exotic state of matter, where no spontaneous symmetry breaking is observed, while a spin-gap is present. It corresponds to a spin-liquid RVB state in the intermediate coupling regime

in the vicinity of the Mott transition.

### **Further insight into the RVB state**

The QMC results presented above uncover the realization of a quantum spin-liquid state of correlated fermions on a non-frustrated, bipartite lattice. In principle, such quantum-disordered states can occur in different flavors, and we thus aim to shed further light on the nature of the spin-liquid observed above. Gapless (algebraic) spin-liquids, or long-range RVB states are characterized by critical spin-spin correlations<sup>9,33–36</sup>. The observation of a finite spin-gap clearly excludes such candidate states, while being consistent with the characterization of the observed spin-liquid in terms of short-range RVB states<sup>17,18,20–22</sup>, also in accordance with the observed short-ranged dimer-dimer correlations. Short-range RVB states are modeled in general by quantum dimer models<sup>21–23</sup>, which capture the fluctuations of singlets in a RVB state, with dimers being a strong-coupling representation of nearest-neighbour singlets<sup>21</sup>. Depending on the lattice geometry, quantum dimer models can exhibit a fully gapped short-range RVB phase, as e.g. on the triangular lattice<sup>37</sup>, but also exhibit spin liquid states with gapless excitations, as is the case for bipartite lattices at the Rokhsar-Kivelson point<sup>21</sup> and within the U(1) spin-liquid phase stabilized for spatial dimensions  $d > 2$ <sup>38</sup>. In the later case, gapless singlet excitations constitute an emerging “photon” soft mode. Fully gapped phases of quantum dimer models are furthermore characterized by a non-trivial topological order, implying e.g. an emerging ground-state degeneracy of two-dimensional systems with periodic boundary conditions in the TDL<sup>23,39</sup>.

In order to assess, whether topological order can characterize the short-range RVB in our case, we examine the low-energy singlet excitations. As proven in an exact theorem by Lieb<sup>40</sup>,



the finite systems used in our numerical simulations have a non-degenerate singlet ground-state for any finite value of  $U > 0$ . Hence, degeneracy can only appear in the TDL. If so, low-energy singlet states should be present, with decreasing excitation energy as the system size increases. Since our QMC method projects out the finite system's ground-state from a singlet trial wavefunction, we can monitor the expectation value of the internal energy  $E(\Theta)$ , where  $\Theta$  is the projection parameter (cf. Methods). Here all contributions from singlet states with the same quantum numbers as the ground-state are included, that have a finite overlap with the trial wave function. For a given system of size  $N$ , we define  $\Theta^*$  as the value of the projection parameter, such that  $(E(\Theta) - E_0)/N < \epsilon$ , for  $\Theta > \Theta^*$ , where  $E_0$  is the ground-state energy, and  $\epsilon$  is an energy scale which we choose small enough, in order to guarantee that  $\epsilon \ll (E_1 - E_0)/N$ , where  $E_1$  is the lowest singlet excited state above the ground-state. Typically, we choose  $\epsilon$  of the order of our statistical error in the energy density. Then,  $1/\Theta^*$  is a lower bound for the lowest singlet excitation (cf. SI). Such an analysis on various lattice sizes leads to the conclusion, that the singlet excitation gap stays above the spin gap in the TDL (cf. SI), providing no evidence for the emergence of a topological state. However, we cannot definitely exclude topological order, if the relevant singlet states happen to have a vanishing overlap with our trial wave function. For the future, it will be interesting to explore the low-energy singlets beyond the projective scheme, and probe for soft modes similarly as does e.g. the construction of finite momentum trial states in quantum dimer models<sup>21,23</sup>. Our findings, based on a controlled numerical framework, therefore open a new facet of quantum spin-liquids, where an appreciable amount of doubly-occupied sites are present, extending well beyond the regime of localized spin physics.

## Discussion and outlook

The presence of a spin-liquid in the Hubbard model on the bipartite honeycomb lattice close to an antiferromagnetic Mott insulator resembles the situation in the organic antiferromagnet  $\kappa$ -(BEDT-TTF)<sub>2</sub>Cu<sub>2</sub>(CN)<sub>3</sub>, which has been argued to display a spin-liquid state<sup>41,42</sup>, albeit the latter system is on a triangular lattice and hence frustrated. This difference can be reconciled starting from the strong-coupling limit of the Hubbard model, i.e. a nearest-neighbour Heisenberg model, that close to the Mott transition acquires corrections that induce efficient frustrations to the spin degrees of freedom. In fact, a Klein Hamiltonian for a spin-liquid state on the honeycomb lattice was constructed, including extended exchange interactions<sup>43</sup>. A more pronounced difference is the appearance of superconductivity in the organic systems upon pressure, that is equivalent to a reduction of the ratio  $U/t$  in the Hubbard model<sup>44</sup>. The absence of superconductivity in our system could be due to the vanishing density of states at the Fermi energy. In this case, a finite coupling strength is needed, at least in the BCS-frame<sup>45</sup>. However, having an unexpected realisation of a short-range RVB state, it would be highly interesting to explore the consequences of doping, in a spirit rather close to the original scenario proposed by Anderson<sup>19</sup> and Kivelson *et al.*<sup>20</sup> for the cuprates. In particular, for the fully gapped short-range RVB state, the finite spin-gap sets the energy scale of pairing in the superconducting state<sup>20</sup>. In this respect, the value obtained for the spin-gap is rather promising. The largest value attained is  $\Delta_s \sim 0.025t$  (Fig. 1), that for  $t$  in the range of 1.5 to 2.5 eV (in graphene is  $t = 2.8$  eV<sup>6</sup>) corresponds to a temperature scale ranging from 400 to 700 K.

Although studies of doping are beyond the power of our quantum Monte Carlo approach due to the sign problem, they could open interesting perspectives e.g. in future experiments with ultra-

cold atoms on a honeycomb optical lattice, or with honeycomb lattices based on group IV elements like expanded graphene (to enhance the ratio  $U/t$ ) or Si, where the nearest neighbour distance is expected to be approximately 50% larger than in graphene<sup>24</sup>, such that correlations effects are enhanced. In fact, first attempts succeeded in synthesizing single-crystal silicon monolayers<sup>46</sup>.

## Methods Summary

At half-filling, the finite- $U$  region can be studied using the determinantal projective QMC algorithm to obtain ground-state expectation values of a physical observable by performing an imaginary time evolution of a trial wave function that is required to be nonorthogonal to the ground-state. The value  $\Theta$  reached in the imaginary time evolution corresponds to a projection parameter<sup>47–49</sup>. For a spin-singlet trial wave function, we found  $\Theta = 40/t$  to be sufficient to obtain converged ground-state quantities within statistical uncertainty. In the presented simulations, we used a finite imaginary time step  $\Delta\tau = 0.05/t$ . We verified by extrapolating  $\Delta\tau \rightarrow 0$  that this finite imaginary time step produces no artifacts. Simulations were performed for systems of linear size  $L = 3, 6, 9, 12, 15$  and  $18$  with  $N = 2L^2$  sites. For periodic boundary conditions these clusters all have nodal  $K$ -points and hence allow a smooth extrapolation to the TDL. Imaginary time displaced quantities are obtained by using the approach in Ref. 50.

1. Weinberg, S. *The Quantum Theory of Fields, Vol. 1: Foundations* (Cambridge University Press, Cambridge, United Kingdom, 2005).
2. Novoselov, K., *et al.* Two-dimensional gas of massless Dirac fermions in graphene. *Nature* **438**, 197–200 (2005).
3. Zhang, Y., Tan, Y.-W., Stormer, H., and Kim, P. Experimental observation of the quantum Hall

- effect and Berry's phase in graphene. *Nature* **438**, 201–204 (2005).
4. Zhang, H., *et al.* Topological insulators in  $\text{Bi}_2\text{Se}_3$ ,  $\text{Bi}_2\text{Te}_3$  and  $\text{Sb}_2\text{Te}_3$  with a single Dirac cone on the surface. *Nat. Phys* **5**, 438–442 (2009).
  5. Chen, Y. L., *et al.* Experimental Realization of a Three-Dimensional Topological Insulator,  $\text{Bi}_2\text{Te}_3$ . *Science* **325**, 178–181 (2009).
  6. Castro Neto, A. H., Guinea, F., Peres, N. M. R., Novoselov, K. S., and Geim, A. K. The electronic properties of graphene. *Rev. Mod. Phys.* **81**, 109–162 (2009).
  7. Herbut, I. F. Interactions and Phase Transitions on Graphene's Honeycomb Lattice. *Phys. Rev. Lett.* **97**, 146401 (2006).
  8. Drut, J. E. and Lähde, T. A. Is Graphene in Vacuum an Insulator? *Phys. Rev. Lett.* **102**, 026802 (2009).
  9. Lee, P. A., Nagaosa, N., and Wen, X.-G. Doping a Mott insulator: Physics of high-temperature superconductivity. *Rev. Mod. Phys.* **78**, 17–85 (2006).
  10. Jördens, R., Strohmaier, N., Günter, K., Moritz, H., and Esslinger, T. A Mott insulator of fermionic atoms in an optical lattice. *Nature* **455**, 204–207 (2008).
  11. Schneider, U., *et al.* Metallic and Insulating Phases of Repulsively interacting Fermions in a 3D optical lattice. *Science* **322**, 1520–1525 (2008).
  12. Lee, S.-S. and Lee, P. A. U(1) Gauge Theory of the Hubbard Model: Spin Liquid states and possible application to  $\kappa$ -(BEDT-TTF) $_2\text{Cu}_2(\text{CN})_3$ . *Phys. Rev. Lett.* **95**, 036403 (2005).
  13. Hermele, M. SU(2) gauge theory of the Hubbard model and application to the honeycomb lattice. *Phys. Rev. B* **76**, 035125 (2007).

14. Raghu, S., Qi, X.-L., Honerkamp, C., and Zhang, S.-C. Topological Mott Insulators. *Phys. Rev. Lett.* **100**, 156401 (2008).
15. Kane, C. L. and Mele, E. J. Quantum spin Hall effect in Graphene. *Phys. Rev. Lett.* **95**, 226801 (2005).
16. Uchoa, B. and Castro Neto, A. H. Superconducting States of Pure and Doped Graphene. *Phys. Rev. Lett.* **98**, 146801 (2007).
17. Anderson, P. W. Resonating valence bonds: A new kind of insulator? *Mater. Res. Bull.* **8**, 153–160 (1973).
18. Fazekas, P. and Anderson, P. W. On the ground state properties of the anisotropic triangular antiferromagnet. *Philos. Mag.* **30**, 432 (1974).
19. Anderson, P. W. The Resonating Valence Bond State in  $\text{La}_2\text{CuO}_4$  and Superconductivity. *Science* **235**, 1196–1198 (1987).
20. Kivelson, S. A. and Rokhsar, D. S. and Sethna, J. P. Topology of the resonating valence-bond state: Solitons and high- $T_c$  superconductivity. *Phys. Rev. B* **35**, 8865–8868 (1987).
21. Rokhsar, D. S. and Kivelson, S. A. Superconductivity and the Quantum Hard-Core Dimer Gas. *Phys. Rev. Lett.* **61**, 2376–2379 (1988).
22. Moessner, R. and Sondhi, S. L. and Fradkin, E. Short-ranged resonating valence bond physics, quantum dimer models, and Ising gauge theories. *Phys. Rev. B* **65**, 024504 (2001).
23. Moessner, R. and Raman K. S. Quantum dimer models. Preprint at <http://www.arxiv.org/abs/0809.3051> (2008).

24. Cahangirov, S., Topsakal, M., Aktürk, E., Şahin, H., and Ciraci, S. Two- and One-Dimensional Honeycomb Structures of Silicon and Germanium. *Phys. Rev. Lett.* **102**, 236804 (2009).
25. Duan, L.-M., Demler, E., and Lukin, M. Controlling Spin Exchange Interactions of Ultracold Atoms in Optical Lattices. *Phys. Rev. Lett.* **91**, 090402 (2003).
26. Sorella, S. and Tosatti, E. Semi-metal-Insulator Transition of the Hubbard Model in the Honeycomb Lattice. *Europhys. Lett.* **19**, 699–704 (1992).
27. Paiva, T., Scalettar, R. T., Zheng, W., Singh, R. R. P., and Otimaa, J. Ground-state and finite-temperature signatures of quantum phase transitions in the half-filled Hubbard model on a honeycomb lattice. *Phys. Rev. B* **72**, 085123 (2005).
28. Ryu, S., Mudry, C., Hou, C.-Y., and Chamon, C. Masses in graphene-like two-dimensional electronic systems: topological defects in order parameters and their fractional exchange statistics. *Phys. Rev. B* **80**, 205319 (2009).
29. Haldane, F. D. M. Model for a Quantum Hall Effect without Landau Levels: Condensed-Matter Realization of the "Parity Anomaly". *Phys. Rev. Lett.* **61**, 2015–2018 (1988).
30. Assaad, F. F., Hanke, W., and Scalapino, D. J. Flux quantization in the two-dimensional repulsive and attractive Hubbard models. *Phys. Rev. Lett.* **71**, 1915–1918 (1993).
31. Byers, N. and Yang, C. N. Theoretical Considerations Concerning Quantized Magnetic Flux in Superconducting Cylinders. *Phys. Rev. Lett.* **7**, 46–49 (1961).
32. Pauling, L. *The Nature of the Chemical Bond*. (Cornell University Press, Ithaca, NY, 1960).
33. Rantner W. and Wen X. G. Spin correlations in the algebraic spin liquid: Implications for high  $T_c$  superconductors. *Phys. Rev. B* **66**, 144501 (2002).

34. Hermele, M. *et al.* On the stability of U(1) spin liquids in two dimensions. *Phys. Rev. B* **70**, 214437 (2004).
35. Assaad, F. F. Phase diagram of the half-filled two-dimensional SU(N) Hubbard-Heisenberg model: a quantum Monte Carlo study. *Phys. Rev. B* **71**, 075103 (2005).
36. Mizusaki, T. and Imada, M. Gapless quantum spin liquid, stripe, and antiferromagnetic phases in frustrated Hubbard models in two dimensions. *Phys. Rev. B* **74**, 014421 (2006).
37. Moessner, R. and Sondhi, S. L. Resonating Valence Bond Phase in the Triangular Lattice Quantum Dimer Model. *Phys. Rev. Lett.* **86**, 1881–1884 (2001).
38. Fradkin, E. and Huse, D. A. and Moessner, R. and Oganesyan, V. and Sondhi, S. L. Bipartite Rokhsar-Kivelson points and Cantor deconfinement. *Phys. Rev. B* **69**, 224415 (2004).
39. Wen, X. G. Mean-field theory of spin-liquid states with finite energy gap and topological orders. *Phys. Rev. B* **44**, 2664–2672 (1991).
40. Lieb, E. H. Two Theorems on the Hubbard Model *Phys. Rev. Lett.* **62**, 1201–1204 (1989).
41. Shimizu, Y., Miyagawa, K., Kanoda, K., Maesato, M., and Saito, G. Spin Liquid State in an Organic Mott Insulator with a Triangular Lattice. *Phys. Rev. Lett.* **91**, 107001 (2003).
42. Yamashita, M., *et al.* Thermal-transport measurements in a quantum spin-liquid state of the frustrated triangular magnet  $\kappa$ -(BEDT-TTF)<sub>2</sub>Cu<sub>2</sub>(CN)<sub>3</sub>. *Nat. Phys.* **5**, 44–47 (2009).
43. Chayes, J. T., Chayes, L., and Kivelson, S. A. Valence bond ground states in a frustrated two-dimensional spin-1/2 Heisenberg antiferromagnet. *Commun. Math. Phys.* **123**, 53–83 (1989).
44. Nam, M.-S., Ardavan, A., Blundell, S. J., and Schlueter, J. A. Fluctuating superconductivity in organic molecular metals close to the Mott transition. *Nature* **449**, 584–587 (2007).

45. Kopnin, N. B. and Sonin, E. B. BCS superconductivity of Dirac electrons in graphene layers. *Phys. Rev. Lett.* **100**, 246808 (2008).
46. Nakano, H., *et al.* Soft Synthesis of Single-Crystal Silicon Monolayer Sheets. *Angew. Chem.* **118**, 6451–6454 (2006).
47. Sugiyama, G., and Koonin, S. E. Auxiliary field Monte-Carlo for quantum many-body ground states. *Ann. Phys.* **168**, 1–26 (1986).
48. Furukawa, N. and Imada, M. Optimization of initial state vector in the ground state algorithm of lattice fermion simulations. *J. Phys. Soc. Jpn.* **60**, 3669–3674 (1991).
49. Assaad, F. F. and Evertz, H. G. *Computational Many-Particle Physics, Lecture Notes in Physics 739*. (Springer-Verlag, Berlin, 2008).
50. Feldbacher, M. and Assaad, F. F. Efficient calculation of imaginary-time-displaced correlation functions in the projector auxiliary-field quantum Monte Carlo algorithm. *Phys. Rev. B* **63**, 073105 (2001).

**Supplementary Information** is attached after the section **Methods**.

**Acknowledgements** We thank L. Balents, S. Capponi, A. H. Castro Neto, A. Georges, M. Hermele, A. Läuchli, E. Molinari, Y. Motome, S. Sachdev, K. P. Schmidt and S. Sorella for discussions. We are grateful to S. A. Kivelson for thoroughly reading our manuscript and providing important suggestions. F.F.A. is grateful to the KITP Santa Barbara for hospitality and acknowledges support by the DFG through AS120/4 and FG1162. A.M. thanks the Aspen Center for Physics for hospitality and acknowledges partial support by the DFG through SFB/TRR21. S. W. acknowledges support by the DFG through SFB/TRR21 and WE3649. We thank NIC Jülich, HRL Stuttgart, the BW Grid and the LRZ München for the allocation of CPU time.



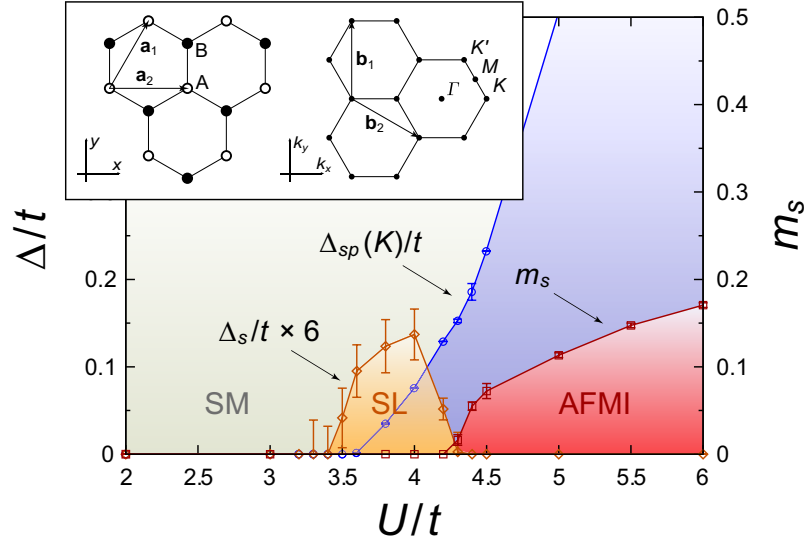


**Figure 1 | Phase diagram for the Hubbard model on the honeycomb lattice at half-filling.** The semimetal (SM) and the antiferromagnetic Mott insulator (AFMI) are separated by a gapped spin liquid (SL) phase in an intermediate coupling regime.  $\Delta_{sp}(K)$  denotes the single-particle gap and  $\Delta_s$  the spin gap.  $m_s$  denotes the staggered magnetization whose saturation value is  $1/2$ . Error bars indicate the standard error (s.e.m.). The inset shows the honeycomb lattice with primitive vectors  $\mathbf{a}_1, \mathbf{a}_2$ , and reciprocal lattice vectors  $\mathbf{b}_1, \mathbf{b}_2$ . Open (full) circles for sublattice  $A$  ( $B$ ), the Dirac points  $K$  and  $K'$ , and the  $M$  and  $\Gamma$  point are indicated.

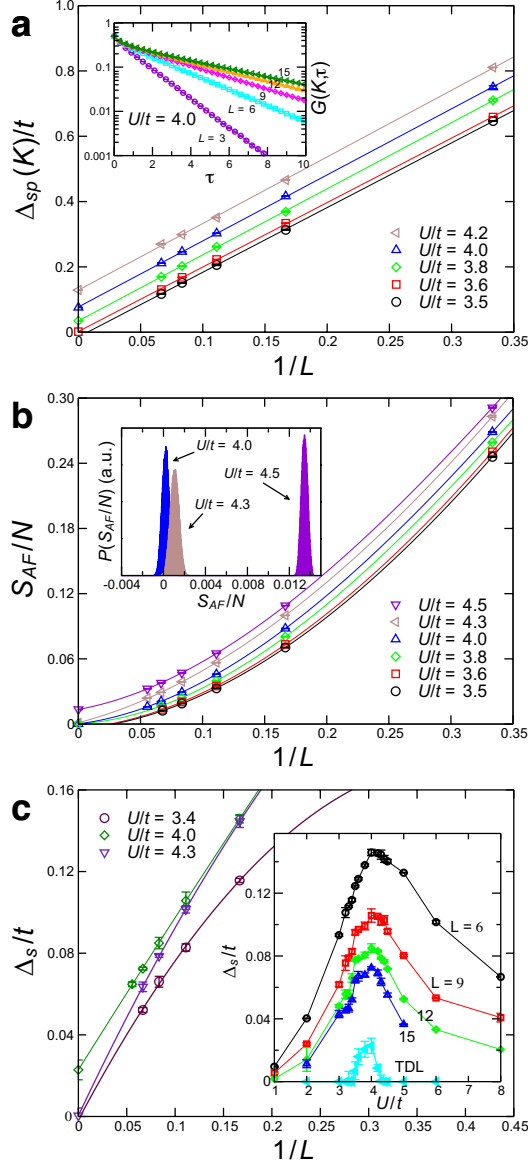


**Figure 2 | Finite size extrapolations of the excitation gaps and the antiferromagnetic structure factor.** **a**, Single-particle gap at the Dirac point  $\Delta_{sp}(K)$  for different values of  $U/t$ , linear in  $1/L$ .  $\Delta_{sp}(K)$  is obtained by fitting the tail of the Green's function (inset) to the form  $e^{-\tau\Delta_{sp}(K)}$ . **b**, Antiferromagnetic structure factor  $S_{AF}$  for various values of  $U/t$  using 3rd order polynomials in  $1/L$ . AF order appears beyond  $U/t = 4.3$ , as seen in the histograms from a Monte Carlo bootstrapping analysis (inset). **c**, Spin gap  $\Delta_s$  at different values of  $U/t$ , using 2nd order polynomials in  $1/L$ . Error bars in **a**, **b**, and **c** indicate the standard error (s.e.m.).

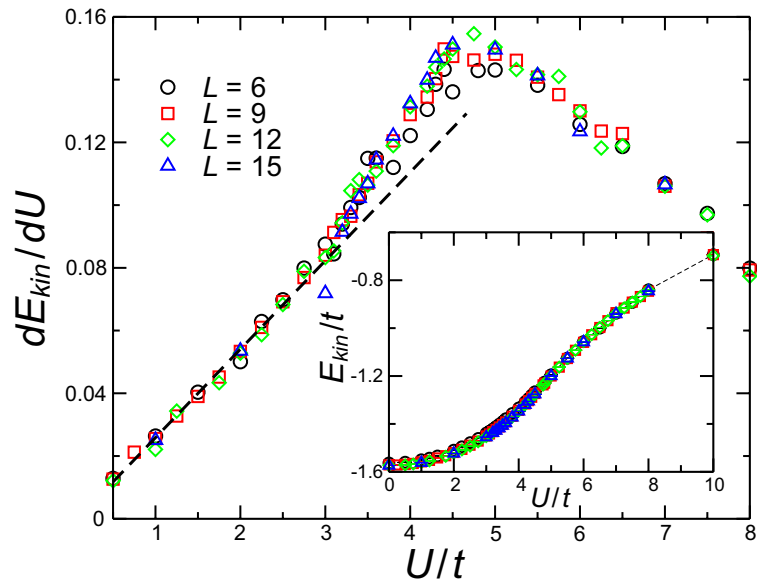


**Figure 3 | Derivative  $dE_{kin}/dU$  of the kinetic energy density as a function of  $U/t$  for systems of different sizes.** The dashed line is a fit to the low- $U$  behaviour. The inset shows the QMC data for the kinetic energy density  $E_{kin}$  from which the derivative is obtained by numerical differentiation. Statistical errors (s.e.m.) are smaller than the symbol size.

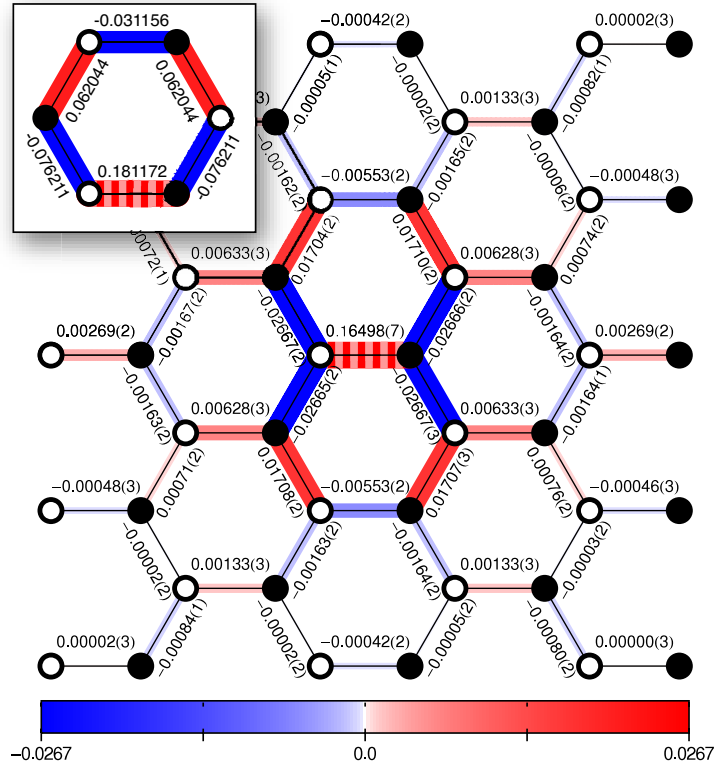


**Figure 4 | Real space plot of the spin dimer-dimer correlations.** The correlation function  $D_{ij,kl}$  (cf. SI) for a  $L = 6$  system at  $U/t = 4$ , together with the same correlation for the isolated Hubbard hexagon also at  $U/t = 4$  (inset). The reference bonds are dressed with stripes. Numbers in parenthesis indicate the standard error (s.e.m.) of the last digit.

## Methods

The projective QMC algorithm employed for the simulations presented in this article constitutes an unbiased, controlled and numerically exact method which is described in detail in Refs. 47,49. Within this scheme, ground-state expectation values of a physical observable  $A$  are obtained from performing an imaginary time evolution

$$\langle A \rangle = \lim_{\Theta \rightarrow \infty} \langle \Psi_T | e^{-\Theta H/2} A e^{-\Theta H/2} | \Psi_T \rangle / \langle \Psi_T | e^{-\Theta H} | \Psi_T \rangle.$$

Here, we used the fact that the ground-state of the Hubbard model on the honeycomb lattice is non-degenerate on any finite lattice at half-filling and for an equal number of sites within the two sublattices<sup>40</sup>, and implicitly assumed that the trial wave function,  $|\Psi_T\rangle$ , has a finite overlap with this ground-state. The standard implementation of the algorithm requires the trial wave function to be a single Slater determinant.

The efficiency of the projective approach strongly depends on the choice of the trial wave function. To generate optimal trial wave functions, different approaches can be employed. One possible strategy consists in optimizing the overlap of the trial wave function with the finite system's ground-state<sup>48</sup>. Alternatively, one can specify a series of good quantum numbers that characterise the ground-state. The trial wave function is then constructed as to share the same quantum numbers. We have chosen the latter approach for our simulations, and generated the trial wave function from the non-interacting tight binding model on a torus, through which we thrust a magnetic flux  $\Phi$ , corresponding to the vector potential  $\mathbf{A} = \Phi \frac{\mathbf{a}_1}{L}$ . In particular, we employed a trial wave function of the form  $|\Psi_T\rangle = |\Psi_T\rangle_{\uparrow} \otimes |\Psi_T\rangle_{\downarrow}$ , where  $|\Psi_T\rangle_{\alpha}$  denotes the ground-state of the single particle Hamiltonian in the spin-flavor  $\alpha$  Hilbert subspace,

$$H_{\alpha}^0 = -t \sum_{\langle i,j \rangle} c_{i,\alpha}^{\dagger} c_{j,\alpha} \exp \left( \frac{2\pi i}{\Phi_0} \int_i^j d\ell \cdot \mathbf{A} \right) + \text{H.c.} .$$

Here,  $\Phi_0 = he/c$  denotes the flux quantum. At  $\Phi = 0$  and for the considered finite lattices of linear size  $L = 3n$  ( $n \in \mathbb{N}$ ), the half-filled ground-state wave function of the above Hamiltonian  $H_\alpha^0$  is degenerate. Imposing an infinitesimal twist (we verified that taking  $\Phi/\Phi_0 = 0.0001$  is sufficiently weak) lifts the two-fold degeneracy of the single particle states at the Dirac points  $K$  and  $K'$ . The thereby produced filled shell configuration guarantees the absence of a negative sign problem, and has total momentum  $K + K' = G$  ( $G$  being a reciprocal lattice vector) and zero total spin. We used this trial wave function for our zero-flux quantum Monte Carlo simulations. Employing this trial wave function, we found an imaginary time projection parameter  $\Theta = 40/t$  to be sufficient to obtain converged ground-state quantities within the statistical uncertainty.

For the presented simulations, we used an  $SU(2)$  symmetric, discrete Hubbard-Stratonovich transformation which allows for a direct generalization of the simulation scheme to  $SU(N)$  symmetric models<sup>35</sup>. In this approach, after performing the standard Trotter-Suzuki decomposition<sup>49</sup>, the interaction part of the imaginary time evolution operator is expressed as

$$e^{-\Delta\tau U(n_\uparrow + n_\downarrow - 1)^2/2} = \sum_{l=\pm 1, \pm 2} \gamma(l) e^{i\sqrt{\Delta\tau U/2} \eta(l)(n_\uparrow + n_\downarrow - 1)} + \mathcal{O}(\Delta\tau^4),$$

with the two functions  $\gamma$  and  $\eta$  of the four-valued auxiliary field  $l = \pm 1, \pm 2$  taking on the values

$$\begin{aligned} \gamma(\pm 1) &= 1 + \sqrt{6}/3, & \eta(\pm 1) &= \pm\sqrt{2(3 - \sqrt{6})}, \\ \gamma(\pm 2) &= 1 - \sqrt{6}/3, & \eta(\pm 2) &= \pm\sqrt{2(3 + \sqrt{6})}. \end{aligned}$$

The advantage of this representation is the fact, that for each Hubbard-Stratonovich configuration, the  $SU(2)$  spin symmetry of the Hubbard model is conserved explicitly. The above Hubbard-Stratonovich transformation produces an overall systematic error proportional to  $\Delta\tau^3$  in the Monte Carlo estimate of observables which, in comparison to the Trotter error of order  $\Delta\tau^2$ , is however negligible. We employed a finite imaginary time step  $\Delta\tau = 0.05/t$  and verified upon extrapolating

$\Delta\tau \rightarrow 0$ , that this value produces no artifacts. In order to extract the gaps to the various excitations of the system, we calculated in addition to equal-time correlations also imaginary time displaced correlation functions. To efficiently calculate these imaginary time displaced quantities, we used an approach that was introduced in Ref. 50, and which accounts for the fact, that for a given auxiliary field configuration the equal-time Green-function matrix is a projector.

Finally, we have confirmed the validity of our implementation against exact diagonalization results on both  $L = 2$  and  $L = 3$  lattices.

## Supplementary Information

In these supplementary sections, we provide further details about the simulation results mentioned in the main text. As a convenient notation, in the following  $c_{\mathbf{x}A\alpha}^\dagger$  and  $c_{\mathbf{x}B\alpha}^\dagger$  ( $c_{\mathbf{x}A\alpha}$  and  $c_{\mathbf{x}B\alpha}$ ) denote creation (annihilation) operators for fermions of spin  $\alpha = \uparrow$  or  $\downarrow$ , on the lattice site that belongs to the sublattice  $A$  and  $B$  respectively, within the unit cell at position  $\mathbf{x}$ . Furthermore,  $n_{\mathbf{x}a\alpha} = c_{\mathbf{x}a\alpha}^\dagger c_{\mathbf{x}a\alpha}$  and  $n_{\mathbf{x}a} = \sum_{\alpha} n_{\mathbf{x}a\alpha}$  denote the local density operators, and  $\mathbf{S}_{\mathbf{x}a} = \frac{1}{2} c_{\mathbf{x}a\alpha}^\dagger \boldsymbol{\sigma}_{\alpha\beta} c_{\mathbf{x}a\beta}$  the local spin operators, where  $\boldsymbol{\sigma} = (\sigma_x, \sigma_y, \sigma_z)$  is the vector of Pauli matrices and  $a \in \{A, B\}$ . The corresponding operators in momentum space are obtained from

$$c_{\mathbf{k}a\alpha} = \frac{1}{L^2} \sum_{\mathbf{x}} e^{-i\mathbf{k}(\mathbf{x}+\mathbf{x}_a)} c_{\mathbf{x}a\alpha}, \quad (2)$$

where  $\mathbf{x}_A = (0, 0)$  and  $\mathbf{x}_B = (0, a)$ , with  $a$  the distance between neighbouring lattice sites. Similarly, Fourier components  $n_{\mathbf{k}a\alpha}$ ,  $n_{\mathbf{k}a}$  and  $\mathbf{S}_{\mathbf{k}a}$  of the density and spin operators are defined. For the following, it is also convenient to introduce the three lattice vectors related to the three nearest neighbour bonds,

$$\boldsymbol{\delta}_1 = (0, 0), \quad \boldsymbol{\delta}_2 = -\mathbf{a}_2, \quad \boldsymbol{\delta}_3 = \mathbf{a}_1 - \mathbf{a}_2,$$

where  $\mathbf{a}_1$  and  $\mathbf{a}_2$  are shown in Fig. 1, as well as

$$\mathbf{r}_1 = \mathbf{a}_2, \quad \mathbf{r}_2 = \mathbf{a}_2 - \mathbf{a}_1, \quad \mathbf{r}_3 = -\mathbf{a}_1, \quad \mathbf{r}_4 = -\mathbf{r}_1, \quad \mathbf{r}_5 = -\mathbf{r}_2, \quad \mathbf{r}_6 = -\mathbf{r}_3$$

connecting a given lattice site to its six next-nearest neighbouring lattice sites. For the correlation between two local operators  $O_1$  and  $O_2$ , we employ a short notation for the cumulant,

$$\langle\langle O_1 O_2 \rangle\rangle := \langle O_1 O_2 \rangle - \langle O_1 \rangle \langle O_2 \rangle. \quad (3)$$

Most of the following results concern the intermediate spin liquid phase, and we present in those cases quantum Monte Carlo data for the representative value of  $U/t = 4$ .



## 1 Green's function and single-particle gap

To probe the single-particle properties, we measured the imaginary-time displaced Green's function

$$G(\mathbf{k}, \tau) = \frac{1}{2} \sum_a \langle c_{\mathbf{k}a\uparrow}^\dagger(\tau) c_{\mathbf{k}a\uparrow}(0) \rangle = \frac{1}{2} \sum_a \langle c_{\mathbf{k}a\downarrow}^\dagger(\tau) c_{\mathbf{k}a\downarrow}(0) \rangle, \quad (4)$$

where  $c_{\mathbf{k}a\alpha}^{(\dagger)}(\tau) = e^{\tau H} c_{\mathbf{k}a\alpha}^{(\dagger)} e^{-\tau H}$ . The single-particle gap  $\Delta_{sp}(\mathbf{k})$  is obtained from  $G(\mathbf{k}, \tau) \propto \exp(-\tau \Delta_{sp}(\mathbf{k}))$  at large imaginary time  $\tau$ , and corresponds to the particle (or hole) excitation energy with respect to the chemical potential  $\mu = 0$  at half-filling in this particle-hole symmetric system. At  $U = 0$ , the single-particle gap vanishes at the Dirac points  $K$  and  $K'$  (cf. Fig. 1 for our notation in momentum space), and we thus considered  $\Delta_{sp}(K)$  in detail. The quantum Monte Carlo data for  $G(K, \tau)$  and  $\Delta_{sp}(K)$  is presented in the main text.

## 2 Spin correlations and $S_{AF}$

The antiferromagnetic order at large values of  $U/t$  resides within the unit cell of the honeycomb lattice. Hence, the spin structure factor for antiferromagnetic order relates to the staggered spin correlations at the  $\Gamma$  point (cf. Fig. 1 for our notation in momentum space),

$$S_{AF} = \langle [\sum_{\mathbf{x}} (\mathbf{S}_{\mathbf{x}A} - \mathbf{S}_{\mathbf{x}B})]^2 / N \rangle. \quad (5)$$

In addition to the above structure factor, we also probed directly the spin-spin correlation functions

$$C_s^{a,b}(\mathbf{x}, \mathbf{y}) = \langle \langle \mathbf{S}_{\mathbf{x}a} \cdot \mathbf{S}_{\mathbf{y}b} \rangle \rangle \quad (6)$$

at the largest available distance  $\mathbf{d}_L = ([L/2 + 1] - 1) \mathbf{a}_1 + ([L/2 + 1] - 1) \mathbf{a}_2$  for different system sizes, and performed a finite size scaling of both  $C_s^{A,A} = C_s^{A,A}(0, \mathbf{d}_L)$  and  $C_s^{A,B} = -C_s^{A,B}(0, \mathbf{d}_L)$ .

A comparison of the scaling of these quantities to  $S_{AF}$  is shown for both  $U/t = 4$  and  $U/t = 4.5$

in Suppl. Fig. 1, exhibiting the consistency between these different approaches to quantify the spin correlations in the ground state.

### 3 Spin excitation gaps

The gaps for spin excitations at momentum vector  $\mathbf{k}$  are obtained from the imaginary-time displaced spin-spin correlation functions for both the staggered sector,

$$S_s(\mathbf{k}, \tau) = \langle\langle (\mathbf{S}_{\mathbf{k}A}(\tau) - \mathbf{S}_{\mathbf{k}B}(\tau)) \cdot (\mathbf{S}_{\mathbf{k}A}(0) - \mathbf{S}_{\mathbf{k}B}(0)) \rangle\rangle, \quad (7)$$

as well as the uniform sector,

$$S_u(\mathbf{k}, \tau) = \langle\langle (\mathbf{S}_{\mathbf{k}A}(\tau) + \mathbf{S}_{\mathbf{k}B}(\tau)) \cdot (\mathbf{S}_{\mathbf{k}A}(0) + \mathbf{S}_{\mathbf{k}B}(0)) \rangle\rangle, \quad (8)$$

where  $\mathbf{S}_{\mathbf{k},a}(\tau) = e^{\tau H} \mathbf{S}_{\mathbf{k},a} e^{-\tau H}$ . Similarly as for the single-particle gap, the spin excitation gaps are obtained from  $S_s(\mathbf{k}, \tau) \propto \exp(-\tau \Delta_s(\mathbf{k}))$ , and  $S_u(\mathbf{k}, \tau) \propto \exp(-\tau \Delta_u(\mathbf{k}))$  at large imaginary time  $\tau$ . The staggered spin gap  $\Delta_s = \Delta_s(\Gamma)$  can be calculated directly via the staggered spin-spin correlations at the  $\Gamma$  point. However, since the total magnetization  $\mathbf{S}_{tot} = \mathbf{S}_{\Gamma A} + \mathbf{S}_{\Gamma B}$  commutes with the Hamiltonian of the system,  $[\mathbf{S}_{tot}, H] = 0$ , the uniform spin gap  $\Delta_u$  cannot be extracted from the uniform spin-spin correlations at the  $\Gamma$  point in a canonical quantum Monte Carlo simulation. Instead, one obtains  $\Delta_u = \lim_{\mathbf{k} \rightarrow \Gamma} \Delta_u(\mathbf{k})$  from measurements performed at the finite momenta closest to the  $\Gamma$  point for each finite system. Supplementary Fig. 2 shows the finite size data for these gaps at  $U/t = 3.3, 4$  and  $4.5$ . For  $U/t = 4$ , both gaps scale to finite values in the thermodynamic limit, with  $\Delta_u$  being about four times as large as  $\Delta_s$ . For the other two values of  $U/t$ , both gaps clearly vanish in the thermodynamic limit.

## 4 Density correlations

The density-density correlation function is given by

$$C_d^{a,b}(\mathbf{x}, \mathbf{y}) = \langle \langle n_{\mathbf{x}a} n_{\mathbf{y}b} \rangle \rangle, \quad (9)$$

where  $a, b \in \{A, B\}$ . At half-filling,  $\langle n_{\mathbf{x}a} \rangle = \langle n_{\mathbf{x}b} \rangle = 1$ . Supplementary Fig. 3 shows the finite size scaling of the density correlations at the largest distance,  $C_d^{A,A} = |C_d^{A,A}(0, \mathbf{d}_L)|$  and  $C_d^{A,B} = |C_d^{A,B}(0, \mathbf{d}_L)|$  at  $U/t = 4$ . Both scale to zero in the thermodynamic limit, and no long-range density correlations persist. Furthermore, in comparison with the spin correlations, the density correlations are seen to be significantly weaker and essentially zero within the statistical error for system sizes  $L \geq 9$ . Consistently, we also find no long-range density ordering when analyzing the density structure factor (not shown).

## 5 Dimer-dimer correlations - charge sector

In this section, we present our results on the dimer-dimer correlations in the charge sector. We measured both the correlations between the kinetic energy bond operators and the current operators. The spin sector is treated in the following section.

Correlations between the kinetic energy bond operators

$$k(\mathbf{x}, a; \mathbf{y}, b) = \sum_{\alpha} (c_{\mathbf{x}a\alpha}^{\dagger} c_{\mathbf{y}b\alpha} + c_{\mathbf{y}b\alpha}^{\dagger} c_{\mathbf{x}a\alpha}), \quad (10)$$

and the current operators

$$j(\mathbf{x}, a; \mathbf{y}, b) = -i \sum_{\alpha} (c_{\mathbf{x}a\alpha}^{\dagger} c_{\mathbf{y}b\alpha} - c_{\mathbf{y}b\alpha}^{\dagger} c_{\mathbf{x}a\alpha}) \quad (11)$$

can be defined between both nearest-neighbour and next-nearest neighbour sites on the honeycomb lattice.

To probe for VBC order in the kinetic energy sector, we measured the three inequivalent dimer-dimer correlation functions

$$C_k^i = |\langle\langle k(0, A; 0, B)k(\mathbf{d}_L, A; \mathbf{d}_L + \boldsymbol{\delta}_i, B) \rangle\rangle|, \quad i = 1, 2, 3, \quad (12)$$

at the largest distance  $\mathbf{d}_L$  on the finite lattices. For an illustration of the different relative bond orientations, see the inset of Suppl. Fig. 4. The upper panel of Suppl. Fig. 4 shows the finite size scaling of the  $C_k^i$  at  $U/t = 4$ . These correlations scale to zero in the thermodynamic limit, hence no long-ranged bond order in the kinetic energy persists. Furthermore, in comparison with the spin correlations, these correlations are also seen to be significantly weaker.

To probe for the persistence of nearest-neighbour currents in the ground state, we measured the current-current correlation functions between the bonds of the honeycomb lattice

$$C_j^i = |\langle\langle j(0, A; 0, B)j(\mathbf{d}_L, A; \mathbf{d}_L + \boldsymbol{\delta}_i, B) \rangle\rangle|, \quad i = 1, 2, 3, \quad (13)$$

at the largest distance  $\mathbf{d}_L$  on the finite lattices. The corresponding finite size scalings are shown in the lower panel of Suppl. Fig. 4. Again, long range correlations in the thermodynamic limit can be clearly excluded, indicating the absence of currents between nearest neighbour sites in the ground state.

To probe for bond order and currents between next-nearest neighbour sites, we measured all inequivalent next-nearest neighbour bond-bond and current-current correlation functions at the largest distances both within the same sublattice and between the two sublattices,

$$C_k^{AA,i} = |\langle\langle k(0, A; \mathbf{r}_1, A)k(\mathbf{d}_L, A; \mathbf{d}_L + \mathbf{r}_i, A) \rangle\rangle|, \quad (14)$$

$$C_j^{AA,i} = |\langle\langle j(0, A; \mathbf{r}_1, A)j(\mathbf{d}_L, A; \mathbf{d}_L + \mathbf{r}_i, A) \rangle\rangle|, \quad (15)$$

$$C_k^{AB,i} = |\langle\langle k(0, A; \mathbf{r}_1, A)k(\mathbf{d}_L, B; \mathbf{d}_L + \mathbf{r}_i, B) \rangle\rangle|, \quad (16)$$

$$C_j^{AB,i} = |\langle\langle j(0, A; \mathbf{r}_1, A)j(\mathbf{d}_L, B; \mathbf{d}_L + \mathbf{r}_i, B) \rangle\rangle|, \quad i = 1, \dots, 6. \quad (17)$$

For an illustration of the different relative bond orientations, see the inset of Suppl. Fig. 5. The quantum Monte Carlo data for the correlations within the same sublattice at  $U/t = 4$  are shown in Suppl. Fig. 5. Both  $C_k^{AA,i}$  and  $C_j^{AA,i}$  all scale to zero in the thermodynamic limit. The corresponding correlations between the two sublattices similarly decay to zero in the thermodynamic limit (not shown). Thus no bond ordering nor currents persist between next-nearest neighbour sites in the ground state at  $U/t = 4$ .

## 6 Dimer-dimer correlations - spin sector

In the spin sector, we measured the dimer-dimer correlation functions

$$D_{ij,kl} = \langle\langle (\mathbf{S}_i \cdot \mathbf{S}_j - \frac{1}{4})(\mathbf{S}_k \cdot \mathbf{S}_l - \frac{1}{4}) \rangle\rangle \quad (18)$$

where  $ij$  and  $kl$  are each nearest neighbour sites on the honeycomb lattice. The quantum Monte Carlo results for these correlations are shown and discussed in the main text.

We furthermore measured correlations between the spin-current operators

$$j_s(\mathbf{x}, a; \mathbf{y}, b) = -i \sum_{\alpha} (-1)^{\alpha} (c_{\mathbf{x}a\alpha}^{\dagger} c_{\mathbf{y}b\alpha} - c_{\mathbf{y}b\alpha}^{\dagger} c_{\mathbf{x}a\alpha}) \quad (19)$$

as well as the spin-bond operators

$$k_s(\mathbf{x}, a; \mathbf{y}, b) = \sum_{\alpha} (-1)^{\alpha} (c_{\mathbf{x}a\alpha}^{\dagger} c_{\mathbf{y}b\alpha} + c_{\mathbf{y}b\alpha}^{\dagger} c_{\mathbf{x}a\alpha}), \quad (20)$$

for next-nearest neighbour sites. We measured these correlations between all inequivalent pairs of next-nearest neighbour sites both within the same sublattice and between the two sublattices at the

largest distance on the finite lattices,

$$C_{s-k}^{AA,i} = |\langle\langle k_s(0, A; \mathbf{r}_1, A) k_s(\mathbf{d}_L, A; \mathbf{d}_L + \mathbf{r}_i, A) \rangle\rangle|, \quad (21)$$

$$C_{s-j}^{AA,i} = |\langle\langle j_s(0, A; \mathbf{r}_1, A) j_s(\mathbf{d}_L, A; \mathbf{d}_L + \mathbf{r}_i, A) \rangle\rangle|, \quad (22)$$

$$C_{s-k}^{AB,i} = |\langle\langle k_s(0, A; \mathbf{r}_1, A) k_s(\mathbf{d}_L, B; \mathbf{d}_L + \mathbf{r}_i, B) \rangle\rangle|, \quad (23)$$

$$C_{s-j}^{AB,i} = |\langle\langle j_s(0, A; \mathbf{r}_1, A) j_s(\mathbf{d}_L, B; \mathbf{d}_L + \mathbf{r}_i, B) \rangle\rangle|, \quad i = 1, \dots, 6. \quad (24)$$

For an illustration of the different relative bond orientations, see the inset of Suppl. Fig. 6. Supplementary Fig. 6 shows the finite size scaling of the correlations within the same sublattice at  $U/t = 4$ . They all decay to zero in the thermodynamic limit. The corresponding correlations between different sublattices show a similar behavior (not shown). Thus no spin-bond order nor spin-currents persist between next-nearest neighbour sites in the ground state at  $U/t = 4$ .

## 7 Flux quantization measurement for superconductivity

In the flux quantization measurement, we thread a magnetic flux  $\Phi$ , in units of the flux quantum  $\Phi_0$ , through the centre of a torus on which the electronic system lies. From the functional form of the ground state energy with respect to the threaded flux,  $E_0(\Phi/\Phi_0)$ , we can distinguish between normal and superconducting ground states. The signature of the latter requires that the macroscopic energy difference  $E_0(\Phi/\Phi_0) - E_0(\Phi/\Phi_0 = 1/2)$  scales in the thermodynamic limit to a periodic function of period  $1/2$ , and the occurrence of an energy barrier between  $\Phi/\Phi_0 = 0$  and  $\Phi/\Phi_0 = 1/2$ . In contrast, a metallic phase is characterized by  $E_0(\Phi/\Phi_0) - E_0(\Phi/\Phi_0 = 1/2)$  vanishing as a power law as a function of system size, while in an insulating phase, it would vanish exponentially. Figure 7 compares the QMC results of the macroscopic energy difference at  $U = 0$  with that at  $U/t = 4$ . In both cases one clearly observes the vanishing of this quantity in the thermodynamic limit. Hence, no signal for superconductivity is obtained from these flux quantization

measurements.

## 8 Order parameters for superconductivity

Order parameters for superconductivity are in principle obtained from considering the irreducible representations of the  $D_6$  point group of the honeycomb lattice, which can be described as a triangular lattice with a basis of two atoms in the sublattices  $A$  and  $B$ , respectively. The Cooper pair wave function of a superconducting state is a product of a spin, orbital and a sublattice component. Since Pauli's principle requires the wave function to be antisymmetric under particle exchange, we obtain the following possibilities for spin-singlet pairing: for an even (odd) orbital part, the wave function must be symmetric (antisymmetric) under sublattice exchange. It is convenient to introduce pair creation operators in the singlet channel

$$\Delta^\dagger(\mathbf{x}, a; \mathbf{y}, b) = c_{\mathbf{x}a\uparrow}^\dagger c_{\mathbf{y}b\downarrow}^\dagger - c_{\mathbf{x}a\downarrow}^\dagger c_{\mathbf{y}b\uparrow}^\dagger, \quad (25)$$

where  $a, b \in \{A, B\}$ . The operator

$$\Delta_s^\dagger(\mathbf{x}) = \frac{1}{2}(\Delta^\dagger(\mathbf{x}, A; \mathbf{x}, A) + \Delta^\dagger(\mathbf{x}, B; \mathbf{x}, B)) \quad (26)$$

describes on-site  $s$ -wave pairing, which is symmetric under sublattice exchange. In Suppl. Fig. 8, we show the  $s$ -wave pair-pair correlation function  $C_\Delta = |\langle \Delta_s(0) \Delta_s^\dagger(\mathbf{d}_L) \rangle|$  at the largest distance at  $U/t = 4$ . No long-ranged pairing correlation sustains to the thermodynamic limit; instead, the on-site pair-pair correlation function decreases rapidly.

Extended pair creation operators based on nearest neighbour pairing can be expressed in terms of phase factors  $f_1^a, f_2^a, f_3^a, a \in \{A, B\}$ ,

$$\Delta^\dagger(\mathbf{x}, f_1^A, f_2^A, f_3^A, f_1^B, f_2^B, f_3^B) = \sum_{i=1}^3 [f_i^A \Delta^\dagger(\mathbf{x}, A; \mathbf{x} + \boldsymbol{\delta}_i, B) + f_i^B \Delta^\dagger(\mathbf{x}, B; \mathbf{x} - \boldsymbol{\delta}_i, A)] \quad (27)$$

For an extended  $s$ -wave,

$$\Delta_{ext.-s}^\dagger(\mathbf{x}) = \Delta^\dagger(\mathbf{x}, 1, 1, 1, 1, 1, 1). \quad (28)$$

Nearest neighbour  $p$ -wave states relate to

$$\Delta_{p_x}^\dagger(\mathbf{x}) = \Delta^\dagger(\mathbf{x}, 0, +1, -1, 0, -1, +1), \quad (29)$$

$$\Delta_{p_y}^\dagger(\mathbf{x}) = \Delta^\dagger(\mathbf{x}, 0, +1, +1, 0, -1, -1), \quad (30)$$

and nearest neighbour  $d$ -wave states to

$$\Delta_{d_{xy}}^\dagger(\mathbf{x}) = \Delta^\dagger(\mathbf{x}, 0, +1, -1, 0, +1, -1), \quad (31)$$

$$\Delta_{d_{x^2-y^2}}^\dagger(\mathbf{x}) = \Delta^\dagger(\mathbf{x}, -2, +1, +1, -2, +1, +1). \quad (32)$$

In terms of next-nearest neighbours, one furthermore obtains the singlet  $f$ -wave state

$$\Delta_f^\dagger(\mathbf{x}) = \sum_{j=i}^6 (-1)^i [\Delta^\dagger(\mathbf{x}, A; \mathbf{x} + \mathbf{r}_i, A) - \Delta^\dagger(\mathbf{x}, B; \mathbf{x} + \mathbf{r}_i, B)]. \quad (33)$$

In order to probe for superconductivity based on nearest neighbour or next-nearest neighbour pairing in the above symmetry sectors, we directly measured in real-space the various inequivalent pair-pair correlation functions at the largest distances on the finite lattices, i.e.

$$C_\Delta^i = |\langle\langle \Delta(0, A; 0, B) \Delta^\dagger(\mathbf{d}_L, A; \mathbf{d}_L + \boldsymbol{\delta}_i, B) \rangle\rangle|, \quad i = 1, 2, 3, \quad (34)$$

for the nearest neighbour pairing states, and

$$C_\Delta^{AA,i} = |\langle\langle \Delta(0, A; \mathbf{r}_1, A) \Delta^\dagger(\mathbf{d}_L, A; \mathbf{d}_L + \mathbf{r}_i, A) \rangle\rangle| \quad (35)$$

$$C_\Delta^{AB,i} = |\langle\langle \Delta(0, A; \mathbf{r}_1, A) \Delta^\dagger(\mathbf{d}_L, B; \mathbf{d}_L + \mathbf{r}_i, B) \rangle\rangle|, \quad i = 1, \dots, 6, \quad (36)$$



for next-nearest neighbour pairing states both within the same sublattice and between the two sublattices. As shown in Suppl. Fig. 9 and Suppl. Fig. 10, both nearest neighbour and next-nearest neighbour pair-pair correlation functions are very weak, even reaching zero within statistical errors for  $L \geq 9$ . From this, we exclude pairing in all the above symmetry sectors, since the full Cooper pair correlations  $\langle \Delta_{ext.-s}(0) \Delta_{ext.-s}^\dagger(\mathbf{d}_L) \rangle$ ,  $\langle \Delta_{p_x}(0) \Delta_{p_x}^\dagger(\mathbf{d}_L) \rangle$ ,  $\langle \Delta_{p_y}(0) \Delta_{p_y}^\dagger(\mathbf{d}_L) \rangle$ ,  $\langle \Delta_{d_{xy}}(0) \Delta_{d_{xy}}^\dagger(\mathbf{d}_L) \rangle$ ,  $\langle \Delta_{d_{x^2-y^2}}(0) \Delta_{d_{x^2-y^2}}^\dagger(\mathbf{d}_L) \rangle$ , and  $\langle \Delta_f(0) \Delta_f^\dagger(\mathbf{d}_L) \rangle$  are linear superpositions of the above pair-pair correlation functions, and hence vanish in the thermodynamic limit. We can thus exclude superconductivity in the half-filled Hubbard model on the honeycomb lattice.

## 9 Lower bound for singlet states in the RVB phase

We consider the internal energy as a function of the projection parameter  $\Theta$ ,

$$E(\Theta) = \frac{\langle \Psi_T | e^{-\Theta H/2} H e^{-\Theta H/2} | \Psi_T \rangle}{\langle \Psi_T | e^{-\Theta H} | \Psi_T \rangle}, \quad (37)$$

where  $|\Psi_T\rangle$  is the trial wave function (cf. Methods). Let  $\{|n\rangle\}$  be the set of eigenstates of  $H$ .

Then, we have

$$E(\Theta) - E_0 = \frac{1}{1 + R(\Theta)} \sum_{n>0} e^{-(E_n - E_0)\Theta} (E_n - E_0) \frac{|\langle n | \Psi_T \rangle|^2}{|\langle 0 | \Psi_T \rangle|^2}, \quad (38)$$

where  $E_0$  is the ground-state energy,  $|0\rangle$  the ground-state, and define

$$R(\Theta) = \sum_{n>0} e^{-(E_n - E_0)\Theta} \frac{|\langle n | \Psi_T \rangle|^2}{|\langle 0 | \Psi_T \rangle|^2}. \quad (39)$$

Next, we consider an energy scale

$$\epsilon \ll (E_1 - E_0)/N, \quad (40)$$

where  $E_1$  is the energy of the first excited singlet with the same quantum numbers as the ground-state, and define  $\Theta^*$ , such that for  $\Theta > \Theta^*$ ,  $(E(\Theta) - E_0)/N < \epsilon$ . Typically,  $\epsilon$  can be taken of the

order of the statistical error in the energy, such that the condition on  $\epsilon$  is clearly fulfilled. However,  $\epsilon$  is not defined in terms of the statistical errors; the only defining condition on  $\epsilon$  is (40). With such a definition we have

$$\epsilon = \frac{1}{N} \sum_{n>0} \frac{e^{-(E_n-E_0)\Theta^*}}{1+R(\Theta^*)} (E_n - E_0) \frac{|\langle n|\Psi_T\rangle|^2}{|\langle 0|\Psi_T\rangle|^2} \ll (E_1 - E_0)/N, \quad (41)$$

such that

$$\frac{R(\Theta^*)}{1+R(\Theta^*)} < \sum_{n>0} \frac{e^{-(E_n-E_0)\Theta^*}}{1+R(\Theta^*)} \frac{(E_n - E_0)}{(E_1 - E_0)} \frac{|\langle n|\psi_T\rangle|^2}{|\langle 0|\psi_T\rangle|^2} \ll 1, \quad (42)$$

so that it also holds that  $R(\Theta^*) \ll 1$ . The last inequality also implies that

$$e^{-(E_1-E_0)\Theta^*} \frac{|\langle 1|\Psi_T\rangle|^2}{|\langle 0|\Psi_T\rangle|^2} \ll 1, \quad (43)$$

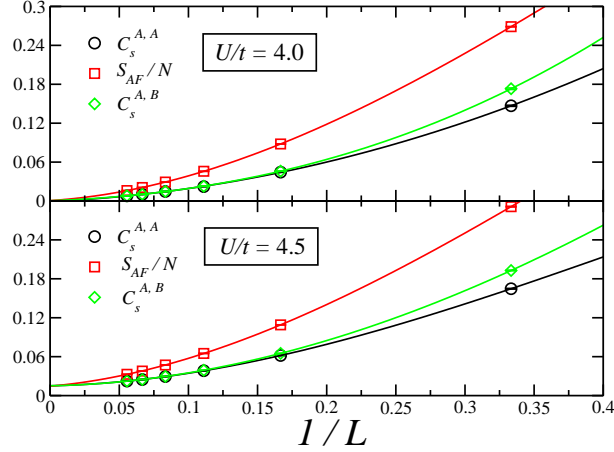
since the sum in  $R(\Theta)$  consists of positive definite terms. In case the overlaps in the last inequality are finite,

$$(E_1 - E_0)\Theta^* \gg 1, \quad (44)$$

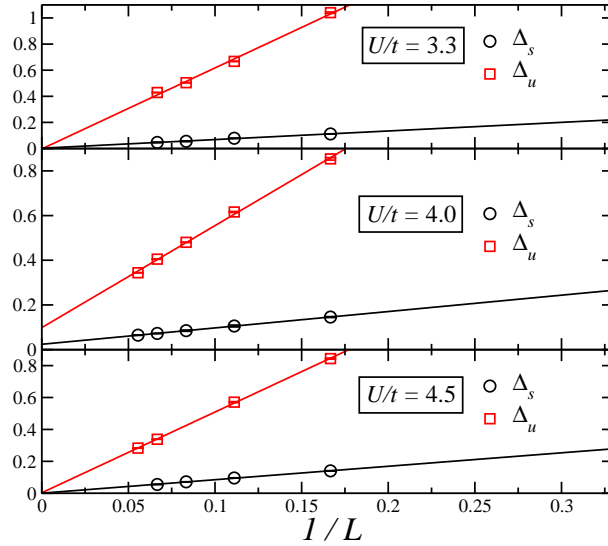
such that  $1/\Theta^*$  provides a lower bound for  $E_1 - E_0$ . In case  $|\langle 1|\Psi_T\rangle|^2/|\langle 0|\Psi_T\rangle|^2 \ll 1$  such that the inequality (43) is fulfilled due to a vanishing overlap, we miss the lowest excited singlet state, and  $1/\Theta^*$  provides a lower bound for the next lowest singlet with a finite overlap with the trial wave function.

For the determination of the lower bound for singlet states we concentrated on the value  $U/t = 4$ , centered in the RVB phase. We verified that in the case  $L = 2$ , where the system can be fully diagonalized, setting  $\epsilon = 10^{-3}t$ ,  $1/\Theta^* = (0.74 \pm 0.04)t$  (s.e.m.) is a lower bound. Namely, for this system size,  $E_1 - E_0 = 1.84t$  for the first excited singlet state of momentum  $\mathbf{k} = 0$ . We also verified that this state has an overlap of 0.22 with the trial wave function. The above value of  $\epsilon$  corresponds to the maximal error for all system sizes. The uncertainty in the determination of  $\Theta^*$  is taken as the maximum between (i) the distance from  $\Theta^*$  to the value of  $\Theta$

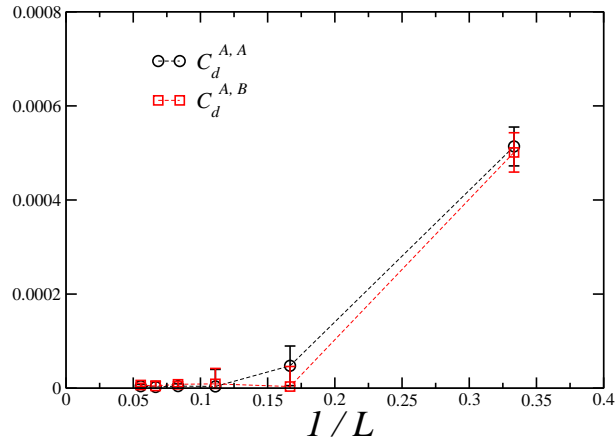
for  $E(\Theta)/N = E(\Theta^*)/N - \epsilon$  and (ii) the distance between two consecutive values of  $\Theta$  around  $\Theta^*$ . By means of error propagation, we then estimate the error in  $1/\Theta^*$ . In Suppl. Fig. 11 we display  $1/\Theta^*$  for  $L = 3, 6, 9,$  and  $12$ , and an extrapolation to the TDL. In all these cases, the lower bound is above the spin-gap, as well as the extrapolation to the TDL. Hence, we find no evidence for singlet states with the same quantum numbers as the ground-state, that may become degenerate with it in the thermodynamic limit. However, this result does not exclude the possibility of low-lying singlet states that have vanishing overlaps with our trial wave function.



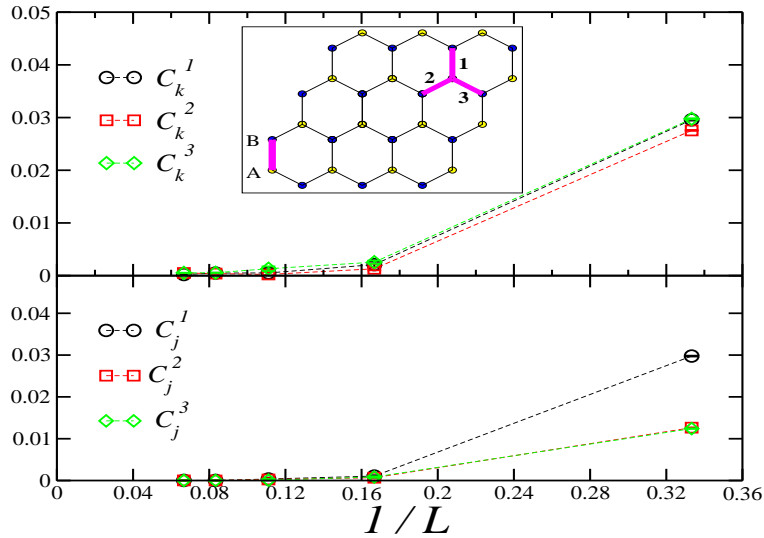
**Supplementary Figure 1** | Comparison of the finite size scaling between the spin correlations  $C_s^{A,A}$  and  $C_s^{A,B}$  at the largest available distance and the staggered structure factor  $S_{AF}$  at  $U/t = 4$  (upper panel) and  $U/t = 4.5$  (lower panel), using 3rd order polynomials in  $1/L$ . Error bars denote standard errors.



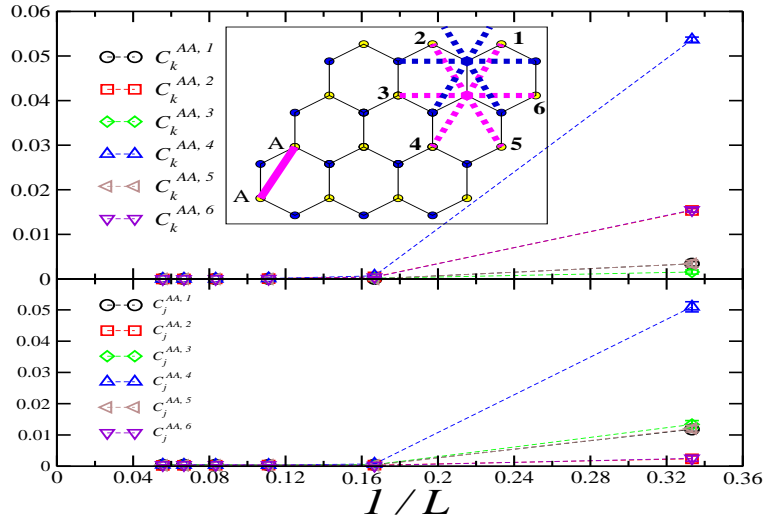
**Supplementary Figure 2** | Comparison of the finite size scaling between the staggered spin gap  $\Delta_s$  and the uniform spin gap  $\Delta_u$  at  $U/t = 3.3, 4$  and  $4.5$  (top to bottom). The extrapolated values in the thermodynamic limit for  $U/t = 4$  are  $\Delta_s = 0.023 \pm 0.007$  (s.e.m.) and  $\Delta_u = 0.099 \pm 0.001$  (s.e.m.). Error bars denote standard errors.



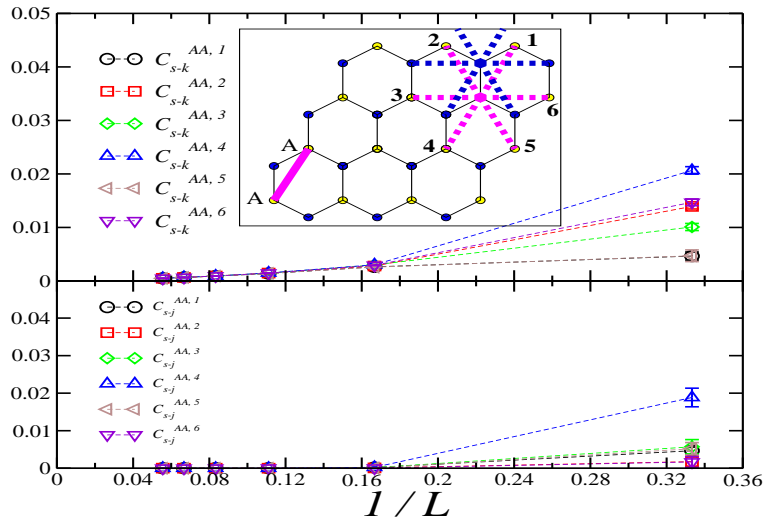
**Supplementary Figure 3** | Finite size scaling of the density correlation functions  $C_d^{A,A}$  and  $C_d^{A,B}$  at  $U/t = 4$ . Error bars denote standard errors.



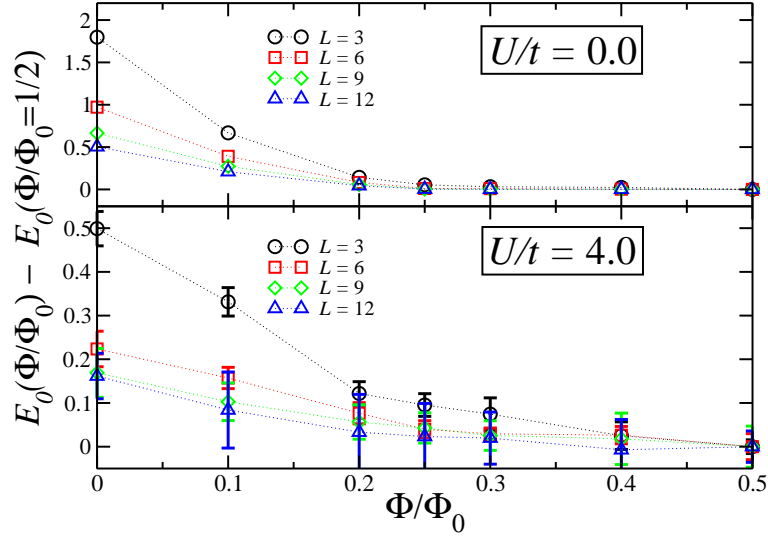
**Supplementary Figure 4** | Finite size scaling of the nearest-neighbour correlations  $C_k^i$  and  $C_j^i$  at  $U/t = 4$ . The inset illustrates the three inequivalent directions with respect to the reference bond marked by  $AB$ . Error bars denote standard errors.



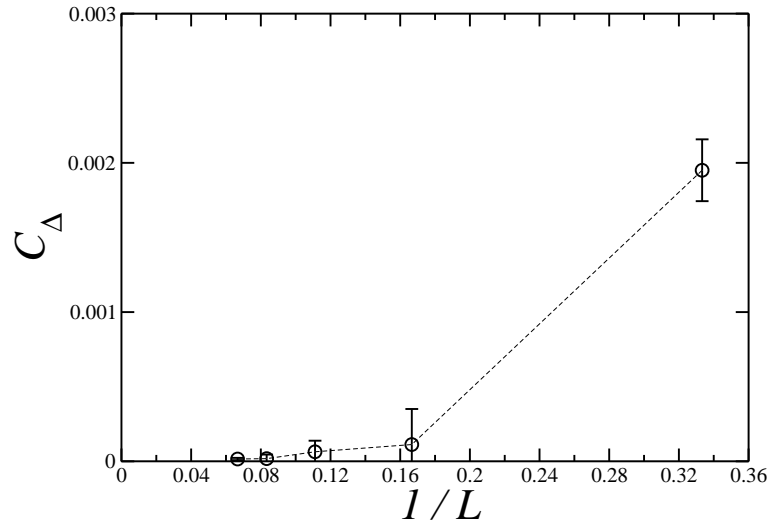
**Supplementary Figure 5** | Finite size scaling of the next-nearest neighbour correlations  $C_k^{AA,i}$  and  $C_j^{AA,i}$  at the largest distance at  $U/t = 4$ . The inset illustrates the inequivalent directions with respect to the reference bond marked by  $AA$ , with the lower (upper) star corresponding to equal (different) sublattices. Error bars denote standard errors.



**Supplementary Figure 6** | Finite size scaling of the next-nearest neighbour correlations  $C_{s-k}^{AA,i}$  and  $C_{s-j}^{AA,i}$  at the largest distance at  $U/t = 4$ . The inset illustrates the inequivalent directions with respect to the reference bond marked by  $AA$ , with the lower (upper) star corresponding to equal (different) sublattices. Error bars denote standard errors.

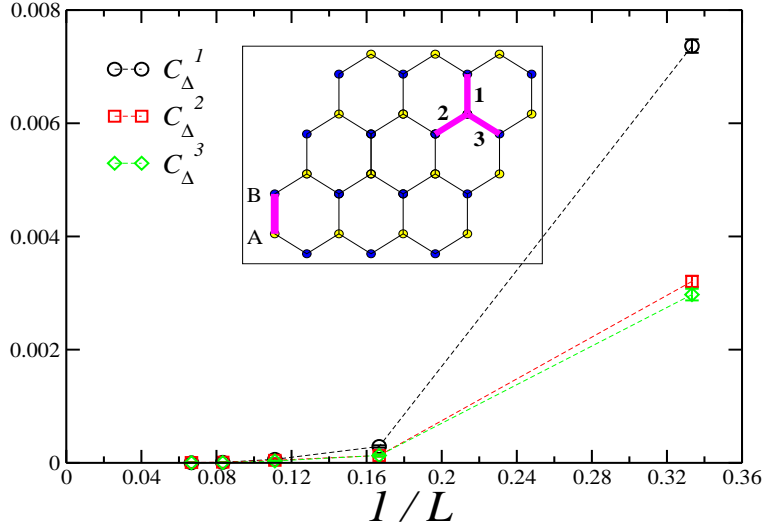


**Supplementary Figure 7** | The energy difference of  $E_0(\Phi/\Phi_0) - E(\Phi/\Phi_0 = 1/2)$  for different system sizes at  $U/t = 0$  and  $U/t = 4$ . Note that the scale for  $U/t = 4$  is four times smaller than for  $U/t = 0$ . The flattening of the energy differences exclude the superconducting ground state at both  $U/t = 0$  and  $U/t = 4$ . Error bars denote standard errors.

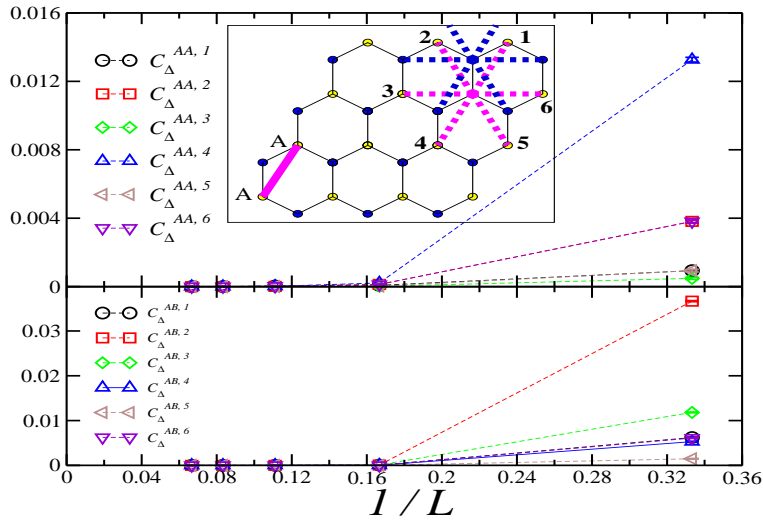


**Supplementary Figure 8** | Finite size scaling of on-site s-wave pairing correlation  $C_\Delta$  at  $U/t = 4$ .

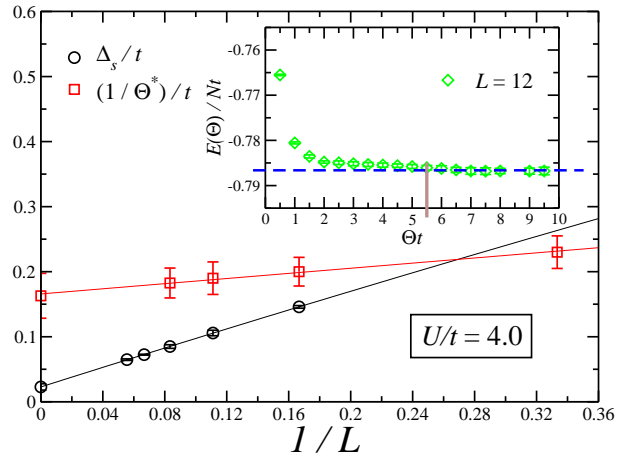




**Supplementary Figure 9** | Finite size scaling of nearest neighbour pair correlation  $C_{\Delta}^i$  at  $U/t = 4$ . The inset illustrates the three inequivalent directions with respect to the reference bond marked by  $AB$ . Error bars denote standard errors.



**Supplementary Figure 10** | Finite size scaling of the next-nearest neighbour pair correlations  $C_{\Delta}^{AA,j}$  and  $C_{\Delta}^{AB,j}$  at  $U/t = 4$ . The inset illustrates the inequivalent directions with respect to the reference bond marked by  $AA$ , with the lower (upper) star corresponding to equal (different) sublattices. Error bars denote standard errors.



**Supplementary Figure 11** | Lower bound  $1/\Theta^*$  for  $L = 3, 6, 9,$  and  $12$  at  $U/t = 4$ . For comparison, the values of the spin-gap are reproduced. The inset shows the internal energy  $E(\Theta)$  as a function of the projection parameter  $\Theta$  for the  $L = 12$  system. The vertical bar gives the position of  $\Theta^*$ . Error bars in  $\Delta_s$  and  $E(\Theta)$  denote standard errors. For the determination of the error bars in  $1/\Theta^*$ , see the text.